eng

MDPI

Article

Development, Designing and Testing of a New Test Rig for Studying Innovative Polycrystalline Diamond Bearings

Alessio Cascino *, Andrea Amedei, Enrico Meli and Andrea Rindi

Department of Industrial Engineering (DIEF), University of Florence, 50121 Florence, Italy; andrea.amedei@unifi.it (A.A.); enrico.meli@unifi.it (E.M.); andrea.rindi@unifi.it (A.R.)
* Correspondence: alessio.cascino@unifi.it

Abstract: This paper reports the preliminary experimental studies carried out on an innovative sliding bearing made of polycrystalline diamond, a material with excellent mechanical and chemical characteristics, used mainly in the drilling industry. Bearings crafted from this material do not necessitate lubrication due to their extremely low coefficient of friction and high resistance to wear. For this reason, they are prime candidates for replacing traditional oil bearings, eliminating the need for auxiliary systems and thereby reducing environmental risks. In this regard, an innovative test rig was designed, capable of reaching speeds up to 6000 rpm both in vertical and horizontal configurations thanks to a novel tilting frame. Moreover, with a high modularity it was possible to test three different kinds of radial PCD bearings. Dynamic data were acquired and elaborated to evaluate orbits, acceleration and absorbed torque, to finally compare these different configurations to better understand how dynamic behavior is influenced by bearings' geometrical characteristics.

Keywords: polycrystalline diamond bearing; rotordynamics; experimental test rig

Citation: Cascino, A.; Amedei, A.; Meli, E.; Rindi, A. Development, Designing and Testing of a New Test Rig for Studying Innovative Polycrystalline Diamond Bearings. *Eng* **2024**, *5*, 1615–1640. https://doi.org/10.3390/eng5030085

Academic Editor: Antonio Gil Bravo

Received: 6 June 2024
Revised: 18 July 2024
Accepted: 23 July 2024
Published: 25 July 2024

1. Introduction

In the introduction, this recent technology is analyzed, discussing the physical properties of the material and the applications of this type of component.

1.1. Polycrystalline Diamond Technology

Synthetic diamond is made of the same material as natural diamonds: pure carbon, crystallized in an isotropic 3D form. It differs from both natural diamond (which is created by geological processes) and diamond simulant (which is made of non-diamond material). Studies on these types of materials are reported in [1–3]. Records of attempted diamond synthesis date back to the turn of the twentieth century. Numerous scientists claimed to have successfully synthesized diamonds between 1879 and 1928, but none were confirmed. In the 1940s, systematic research began in the United States, Sweden and the Soviet Union to grow diamonds, which culminated in the first reproducible synthesis of diamond in 1954. Nowadays, four manufacturing processes have been discovered: Chemical Vapor Deposition synthesis (CVD), High-Pressure High-Temperature synthesis (HPHT), detonation synthesis and high-power ultrasound synthesis. CVD and HPHT processes still dominate the production of synthetics diamonds. The detonation process entered the market in the late 1990s. Here, the detonation of carbon-containing explosives creates nanometer-sized diamond grains. The high-power ultrasound process currently has no commercial application. The properties of synthetic diamond depend on the manufacturing process. However, some synthetic diamonds (whether formed by HPHT or CVD) have properties such as hardness, thermal conductivity and electron mobility that are superior to those of most naturally formed diamonds. Synthetic diamond is widely used in abrasives, in cutting and polishing tools and in heat sinks. Electronic applications of synthetic diamond are being developed, including high-power switches at power stations, high-frequency field-effect

transistors and light-emitting diodes. Synthetic diamond detectors of ultraviolet (UV) light or high-energy particles are used at high-energy research facilities and are available commercially. Because of its unique combination of thermal and chemical stability, low thermal expansion and high optical transparency in a wide spectral range, synthetic diamond is becoming the most popular material for optical windows in high-power CO_2 lasers and gyrotrons. It is estimated that 98% of industrial-grade diamond demand is supplied with synthetic diamonds. In Table 1, some mechanical properties of PCD are reported. Because diamond bonds are so short, they are extremely strong, leading to its very high hardness. Diamond is the hardest known material. It has the highest thermal conductivity of any other material, four times that of copper. Vibrational energy can travel extremely quickly through the lattice. The strength of the bonds resists disruption, giving diamond a high melting point, 500 °C above tungsten. The diamond structure allows sound to propagate at an extreme velocity. It is very stiff, with a coefficient of thermal expansion less than silicon. Diamond has a low coefficient of friction and it is more slippery than teflon. It is chemically inert: acids do not attack it and it is biologically compatible.

Table 1. Extreme properties of diamond.

Property	Value
Density	4–4.35 × 10^6 [kg/m^3]
Young's Modulus	850–1000 [GPa]
Poisson Ratio	0.1
Hardness	50–100 [GPa Knoop]
Thermal Conductivity	500–2000 [W/mK]
Melting Point	4000 [°C]
Sonic Velocity	18,000 [m/s]
Coefficient of Thermal Expansion	1.1 × 10^{-6} [1/K]
Optical Index Refraction	2.42
Coefficient of Friction	0.01–0.07
Biologically Compatible	Pure carbon

1.2. Applications

Most industrial applications of synthetic diamond have long been associated with its hardness. This property makes diamond the ideal material for machine tools and cutting tools, as shown in Figure 1.

Figure 1. Some kinds of PCD drilling tools [4].

As the hardest known naturally occurring material, diamond can be used to polish, cut or wear away any material, including other diamonds. Common industrial applications include diamond-tipped drill bits and saws, and the use of diamond powder as an abrasive. These are by far the largest industrial applications of synthetic diamond. While natural

diamond is also used for these purposes, synthetic HPHT diamond is more popular, mostly because of the better reproducibility of its mechanical properties. Diamond is not suitable for machining ferrous alloys at high speeds, as carbon is soluble in iron at the high temperatures created by high-speed machining, leading to greatly increased wear on diamond tools compared to alternatives. The usual form of diamond in cutting tools is micron-sized grains dispersed in a metal matrix (usually cobalt) sintered onto the tool. This is typically referred to in industry as polycrystalline diamond (PCD). PCD-tipped tools can be found in mining and cutting applications. For the past fifteen years, work has been done to coat metallic tools with CVD diamond, and though the work shows promise, it has not significantly replaced traditional PCD tools. Abrasive particles, high temperatures, corrosive chemicals, and high loads all contribute to failure in bearings used in down-hole drilling tools. Polycrystalline diamond (PCD) bearings outperform other bearing technologies in these harsh conditions due to the unmatched properties of diamond.

PCD bearings are specifically designed to sustain thrust loads, radial loads or a combination of them. Figure 2 illustrates some kinds of PCD bearings. Drilling tool bearing applications include thrust bearing in turbo-drills and thrust or radial bearing in drilling motors, coring tools and power generation turbines. The keys element for a PCD bearing are extreme hardness and high thermal conductivity, which lead to wear resistance and heat removal. In addition, high strength and toughness and low friction make this material very interesting for application on bearings. They simplify equipment and assemblies by eliminating the need for seals and auxiliary lubrication systems. Research on this type of material and its application is focused on wear and abrasion behavior [5–8]. In [9], an important study about life behavior and a lubrication regime is reported. Studies on friction, constant load life and loading capacity are shown for various types of thrust bearings. In [10], a methodology for the designing and building of simple foil thrust bearings intended for parametric performance testing and low marginal costs is described. A test rig for the measurement of the load performance of water-lubricated hydrostatic/hydrodynamic thrust bearings operating under conditions typical of cryogenic turbo pumps (TPs) is reported in [11]. Studies have been carried out mainly on the wear and the life limit of these bearings, without focusing too much on the rotor dynamics aspects, due also to the low speeds in their usual application. One of the characteristic and fundamental aspects of this type of bearing concerns the low dry friction coefficient, which allows it to be used without the aid of synthetic lubricants such as grease and oil. It also has a very high resistance to chemical agents and corrosive environments and can withstand very high loads. The strategic importance that these bearings could have in turbomachinery applications (especially for subsea and remote location oil and gas extraction) becomes immediately evident for various reasons. Some studies about subsea electric pumps are reported in [12,13]. Currently, the most important concerns in subsea applications are represented by higher costs than surface applications with the same system components, both in terms of initial costs and maintenance. For this reason, the possibility of completely removing the auxiliary systems for oil circulation, often very unreliable systems that lead to the interruption of the correct functioning of the machine, is a significant strategic advantage. Furthermore, the use of PCD bearings allows the complete removal of the seals necessary to separate the process fluids from the auxiliary ones; therefore, the use of multiphase machines leads to an increase in the quantity of fluid processed. These machines have very high rotational speeds for the typical applications of these bearings. It is necessary, then, to carry out research aimed at understanding the physical phenomena concerning their behavior and develop a mathematical model that predicts their behavior. With the aim of testing different classes of radial PCD bearings, an innovative test rig was designed. Thanks to its high modularity, three different kinds of radial PCD bearings can be tested. In addition, the test rig has a tilting frame which allows it to reach speeds up to 6000 rpm in both vertical and horizontal configurations.

Figure 2. PCD bearings on the left and real view of PCD bearing samples (rotor and stator rings) on the right.

In the subsequent sections, in addition to the proposed methodology, the design of the bench is described in detail: the mechanical design, transmission system, cooling system, and an overall view of the acquisition systems are appropriately discussed. The experimental results are then presented by processing the acquired data extensively in both the time and frequency domains, considering orbital displacements, torque absorption and frequency response spectrums. Finally, the results are summarized and discussed for each configuration.

2. Materials and Methods

2.1. Methodology

The present activity can be divided into two fundamental parts, one experimental and one numerical, followed by the validation of the numerical model with the experimental data, as briefly summarized in Figure 3. Contact models represent a fundamental aspect of the numerical approach of the project. The selection of an appropriate model for a given contact problem is still an important and challenging issue to be addressed. Some really good reviews of contact force models that are used in the dynamical analysis of multibody systems can be found in [14–16]. The present paper is focused only on the experimental part of the work, with the objective to describe the innovative test rig in detail and present the main results obtained from the experimental test campaign that was carried out.

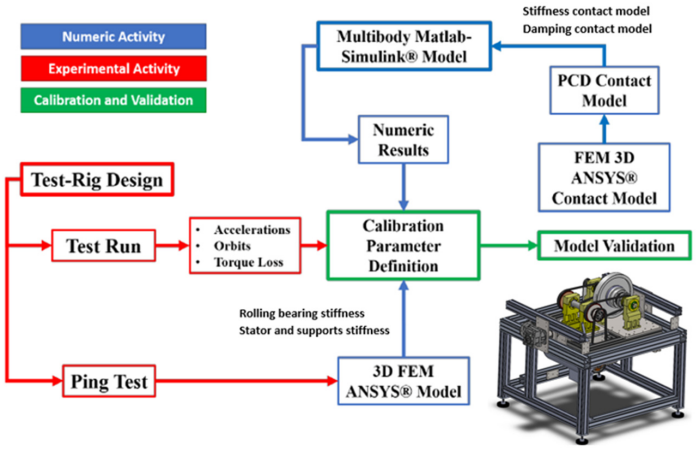

Figure 3. Activity workflow.

The test rig was equipped with various sensors to measure stator accelerations, rotor orbits and the torque absorbed by the PCD bearing. A cooling system was required. Three different types of bearings were tested. The main difference between them is the rotor–stator clearance in the radial direction, from which the name of the testcase is determined: "Baseline" (50 µm), "Low" (40 µm) and "High" (200 µm). Just the "baseline" was tested in the horizontal and vertical configurations. Raw data were acquired and elaborated to understand the behavior of the rotor, as shown within next paragraphs.

2.2. PCD Test Rig Design

The test rig was intended to simulate the behavior of a special design of turbomachinery, in which the individual impellers have independent drives, each driven by a permanent magnet motor, in a configuration with the permanent magnets mounted in the rotor itself, which therefore act as both a motor and an impeller. The main purpose of the test rig was to represent a single rotor in this turbomachinery system, where each rotor was independent from the others, using different kinds of PCD bearings and configurations at several different rotational speeds. The critical parameters and specifications considered during the design of the rig were a maximum main rotor speed of 6000 rpm, modularity, easy variation of rotational axis inclination, decoupling the dynamic behavior of the rotor from the rest of the test rig and rotor inertial properties similar to a real machine. The test rig has a strong integration with heat dissipation and dynamic data acquisition systems. The main physical quantities of interest to better understand the dynamic behavior of the PCD were the rotor displacements (to plot orbits), stator accelerations (to better understand the rotor–stator interaction) and torque on stator, to evaluate the power loss from PCD bearings. The next paragraphs provide a precise and comprehensive explanation of each mechanical component, the cooling circuit and the measurement system, including the specification used when designing the rig and the acquisition system and selecting the instrumentation.

2.3. Mechanical Design

The system is characterized by the presence of a 15 kW electric motor (slow shaft) which, through a secondary transmission shaft, used to avoid a high transmission ratio between low and fast shaft, rotates the disk containing the PCD bearings (the fastest axis) around the main statoric shaft, as shown in Figure 4a. These three axes are supported by steel pedestals, which are bolted to a base plate reinforced with an aluminum frame. A tilting frame is linked to an aluminum fixed frame with two hinges. They allow the base to be tilted easily from a horizontal to a vertical configuration and vice versa, as shown in Figure 4b. The chassis is covered by a steel enclosure that serves as a containment shield in case of failure. Figure 4c illustrates it.

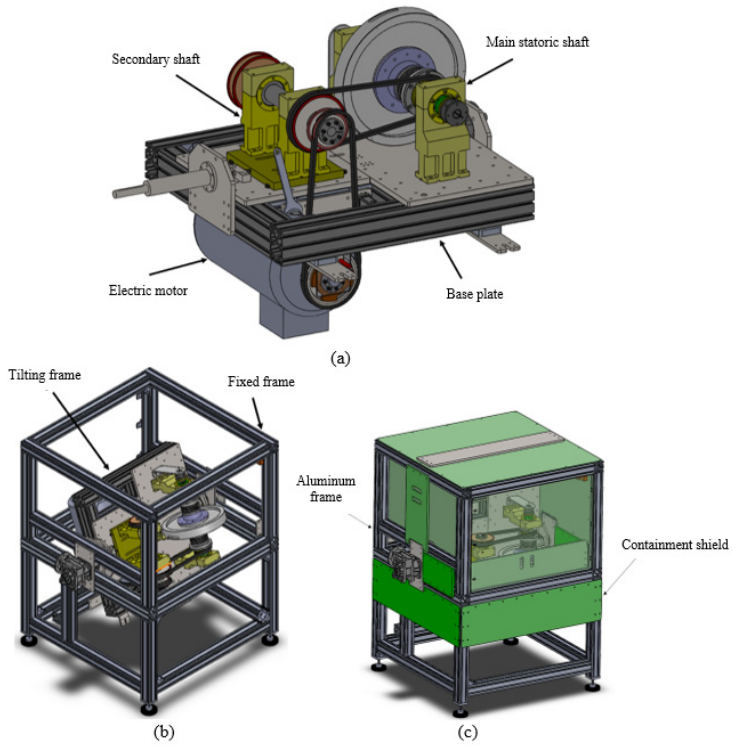

Figure 4. Test rig CAD model overview: (**a**) tilting base with motor, secondary shaft and main axis; (**b**) frame definition; and (**c**) aluminum frame with steel armor.

One of the most difficult goals to achieve was the decoupling of the main rotor from the rest of the test rig. In fact, on the prototype machine the rotors are essentially free to move axially and to rotate around axes perpendicular to the longitudinal axis, until the complete recovery of the clearance. Therefore, one of the requirements of the drive coupling must be to minimize the spring-back forces opposing these degrees of freedom, so that these potential movements can also be represented. The two options explored were an elastic and a magnetic coupling. The main parameters chosen for the execution of the project "trade-off" were the following: the ability of the solution to represent the physics of real-application turbomachines, constructive simplicity, TRL (technology readiness level) and time and costs for finding the component. Table 2 describes how the two options present themselves in relation to the project requirements.

Table 2. Main characteristics of the different transmission systems.

Requirements	Magnetic Joint	Elastic Joint
Representativeness of the solution	Transmission without physical contact.	System able to "decouple" quite effectively.
Constructive simplicity	Simple and space-saving configuration.	Overall dimensions greater than the magnetic coupling.
TRL	Custom component (low TRL).	Known and referenced component.
Time and costs	High, custom product.	Low, standard product.

The two solutions were almost equivalent in their ability to effectively represent the behavior of the real turbomachine. Furthermore, the magnetic coupling had some advantages in terms of simplicity of configuration. However, the TRL and the time and costs associated with procurement oriented the choice to the advantage of the more conventional flexible coupling. Torque transmission is accomplished by a timing pulley–belt system. The number of belts from the secondary shaft to the rotor system depends on the configuration. The horizontal configuration (Figure 5a,c) includes two belts and a symmetric transmission system. Instead, in the vertical configuration (Figure 5b,d), the left belt and pulley system is substituted by an axial PCD bearing to react to the gravitational force, so the torque transmission is provided by a single belt. On the main stationary shaft, the timing pulley is supported on roller bearings, and the torque is transmitted to the rotor by 2 (or 1 in the vertical configuration) high-precision and torsional stiff metal bellow couplings. The main purpose of the metal bellow is to decouple the dynamic response of the rotor (and so the PCD) from the rest of the rotational parts of the test rig. Thanks to the high modularity of the design, changing configurations is a simple and fast procedure.

2.4. Cooling System Design

The cooling system is composed of a 500 L water tank, a recirculation pump and a bypass valve to control the water temperature, measured with a thermocouple, grouped in a simple steel frame (Figure 6). The bypass valve is activated when the temperature is too high in order to mix the high-temperature water with the coolest water inside the tank. During operation, temperatures exceeding 90 °C were never recorded. The system allows the control of the water flow and the temperature. The cooling water enters the PCD bearings through some cavities and channels machined into the stationary shaft. Looking at the cross-section of the main shaft in the vertical configuration in Figure 7a, it is possible to see the water-cooling circuit inside the statoric axis. Blue arrows mean cold water while red arrows mean hot water. An axial channel brings the water from the inlet to the center of the PCD bearing. Then, three radial channels arranged at 120° (visible in Figure 7b) bring the water into a groove just under the PCD and then thirteen holes on the inner ring uniformly distribute the water on the PCD pad, where cooling takes place.

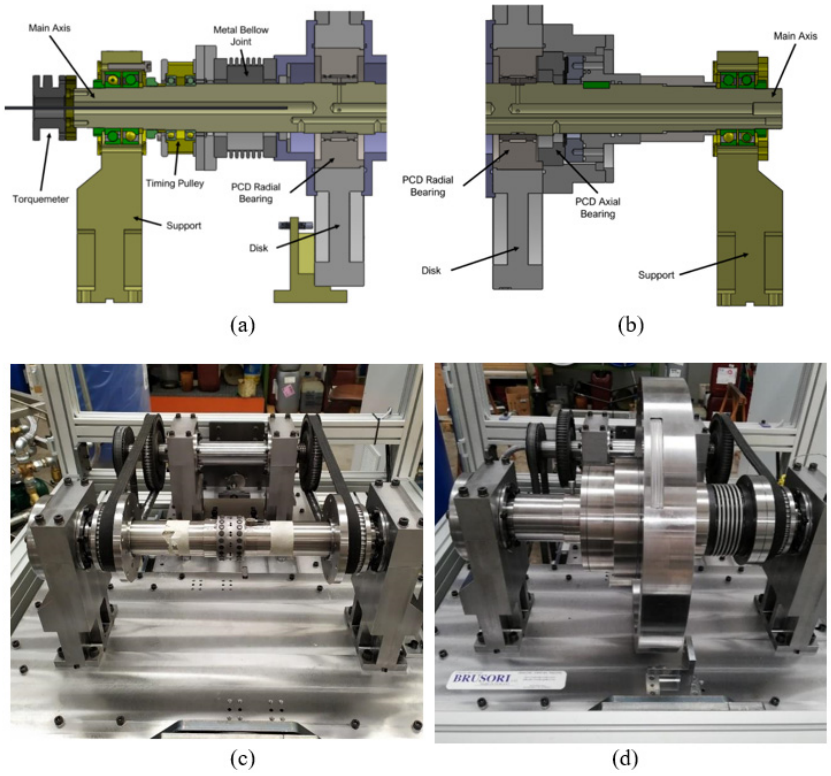

Figure 5. (**a**) Cross-section of partial main axis in horizontal configuration, (**b**) cross-section of partial main axis in vertical configuration, (**c**) torque transmission system: horizontal configuration with symmetric belt–pulley system on main axis, and (**d**) torque transmission system: vertical configuration with asymmetrical transmission system on main axis.

Subsequently, hot water flows into two rotating chambers connected with the outlet channel, thanks to two holes in the lower side of the stationary shaft. The axial PCD cooling circuit is used only for the vertical configuration: cooling water passes through a series of holes and channels until it reaches the axial PCD pads. After cooling action, hot water reaches the same outlet channel as seen for radial PCD cooling in the previously described way (Figure 8).

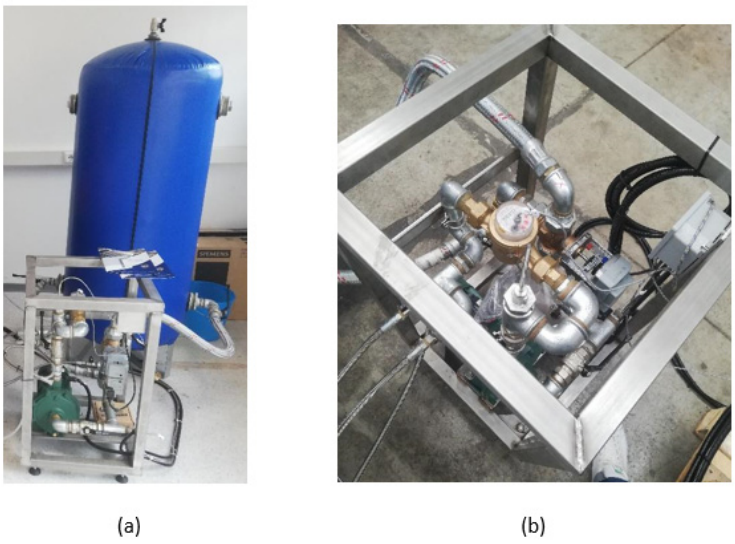

Figure 6. Cooling system: (**a**) cold water tank; (**b**) steel frame with recirculation pump and bypass valve.

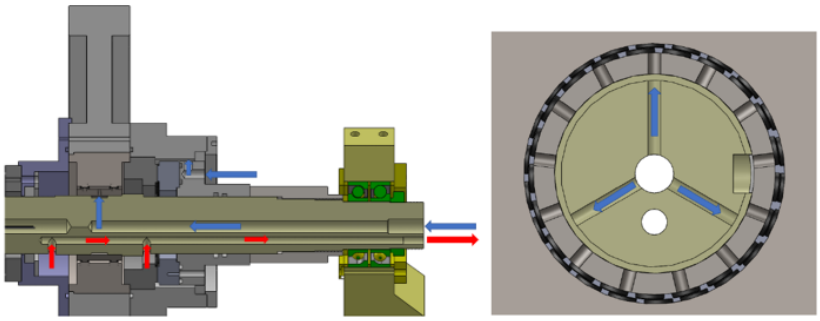

(a) (b)

Figure 7. (**a**) Main axis cross-section (water circulation) and (**b**) mid-plane main axis cross-section: the three radial channels arranged at 120°.

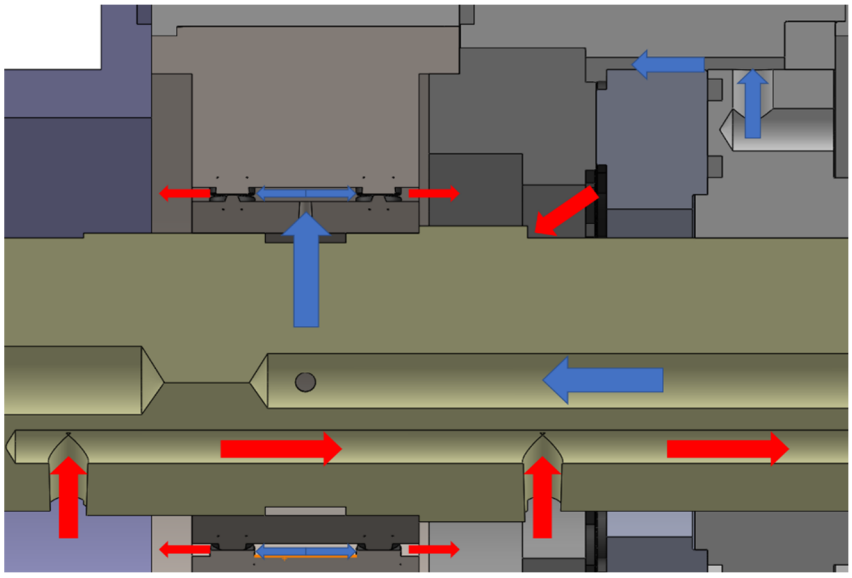

Figure 8. Focus on cooling water flows inside the main shaft: radial and axial PCD cooling. (Blue arrows mean cold water while red arrows mean hot water.)

2.5. Acquisition Data System Design

The aim of the measurement system was to evaluate: the torque and power loss by PCD bearings, acceleration of the support and base and displacement of the rotor (both axial and radial), the orbits and dynamics of the rotor and the radial acceleration induced by the rotor on the stationary shaft, and the exchanged forces during tests, and the PCD temperature. These quantities were measured by the following sensors: 1 torquemeter, 2 external single-axis accelerometers, 2 internal single-axis accelerometers, 4 eddy current sensors (2 radial and 2 axial), 6 thermocouples of type K (TC) for the PCD and 1 thermocouple for cooling system. The torquemeter, visible in Figure 9a with the tag T, is a reaction torquemeter and acts as the torsional constraint for the main axis which is connected to the pedestals via roller bearings. This configuration allows the direct measurement of the PCD bearing reaction torque (the power loss by the roller bearing under the pulley was neglected). Figure 9a also depicts the external accelerometers with the tag Aext1 used to measure the pedestal and base vibrations. The accelerometers are fixed on the main axis with an angular relative position of 90°, as depicted in Figure 9b, as near as possible to the mid-plane of the rotor, to evaluate the acceleration of the main axes when subjected to the forces generated by the rotor. The thermocouples are placed inside the PCD inner ring, as near as possible to the PCD pads, to control and evaluate the effect of friction and the water cooling system.

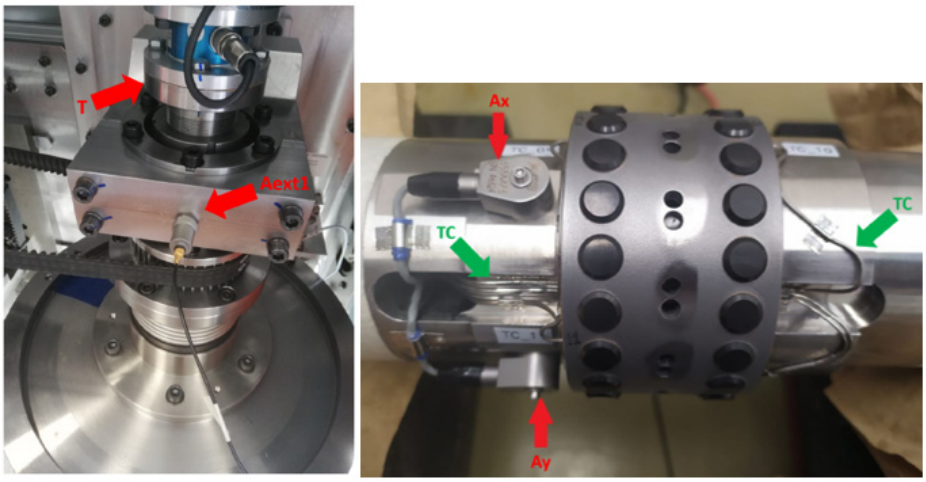

Figure 9. (**a**) Torquemeter (T) and an external accelerometer (Aext1) and (**b**) internal accelerometers (Ax and Ay) and internal thermocouples (TCs).

The probes are positioned by two brackets (Figure 10a) bolted to the base plate. Both radial and axial probes have an angular relative position of 90°. The axial probes face opposite sides of the rotor, so it was possible to characterize the displacement of the rotor. Figure 10b shows a close-up view of one of the proximity probes.

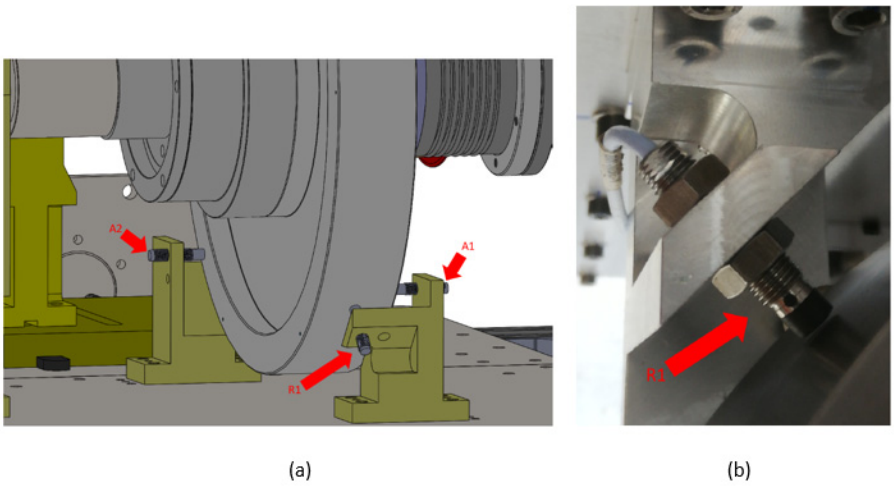

Figure 10. (**a**) Radial (R1) and axial (A1 and A2) proximitors. (**b**) Real position of a radial proximitor (R1).

The dynamic acquisition system (shown in Figure 11) consists of the following: a proximitor for each eddy current probe, a charge amplifier for the external accelerometer and a specific board (NISCB-68) to read signals with the chassis, a chassis (NI PXI 1042) with 2 boards to acquire dynamic signals (NI PXI 4472 and NI PXI 6259 respectively) and 1 board (NI PXI 8336) to communicate with the scientific workstation and a scientific workstation (HP Z720) with a specific board (NI MXI-4) to communicate with the acquiring chassis using an optical fiber.

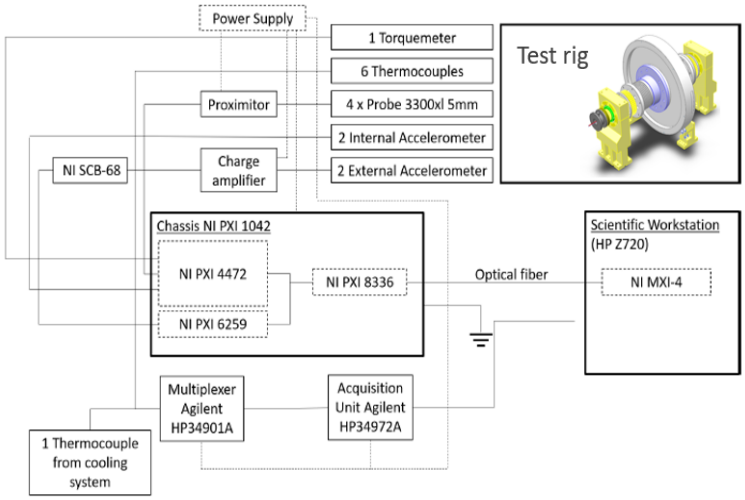

Figure 11. Dynamic acquisition system scheme.

The torquemeter and internal accelerometer are powered directly by one board present in the chassis. The proximity probes and external accelerometer need an independent power supply. To transfer the signal from the acquiring system to the scientific workstation, an optical fiber cable was used.

2.6. Signal Elaboration Workflow

The elaboration of the experimental signals obtained from the test runs of the test rig was divided into 3 main phases: reference system rotation, time series steady-state range selection and filter application.

2.6.1. Reference System Rotation

This transformation was necessary considering that the experimental and numerical results had different reference systems. To be more easily compared, it was necessary to make a rigid rotation of the reference systems and, consequently, of the time series. A scheme representing the cross-section of the center of the test rig is shown in Figure 12. The proximity probes and the accelerometers are represented in blue, with their reference system in red (Ox1y1) and yellow (Ox2y2), respectively, while the numeric reference is in black (Oxy). Note that the sensor reference systems were rotated by 180°. In green are reported two example signals for displacements (r1 and r2) and in orange are reported accelerations (a1 and a2).

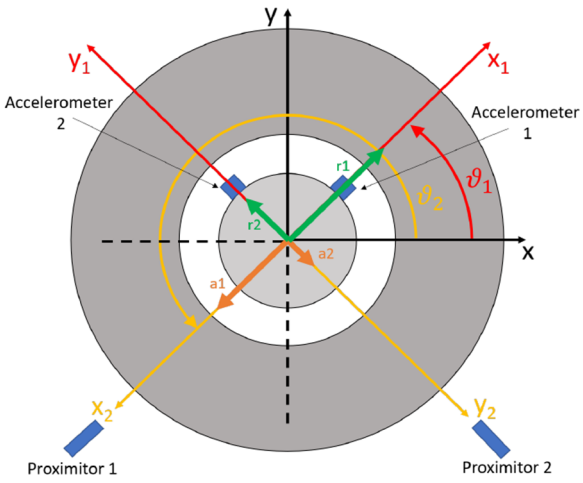

Figure 12. Reference systems' rotation from experimental to numeric.

Considering the scheme described in Figure 12, with the angle θ_1 between the proximitor reference system and the numeric reference system of 45°, with the Equation (1) it was possible to rotate the time series of the rotor displacements:

$$\begin{cases} r_x = r_1 \cos\theta_1 - r_2 \, sin \, \theta_2 \\ r_y = r_1 \ sin\theta_1 + \ r_2 \, cos\theta_1 \end{cases} \quad (1)$$

In Figure 13, an example of proximity signal rotation is shown. In particular, Figure 13a,c illustrate the time series of the x and y proximity probes, respectively. Figure 13b illustrates the effective rotation of the orbit.

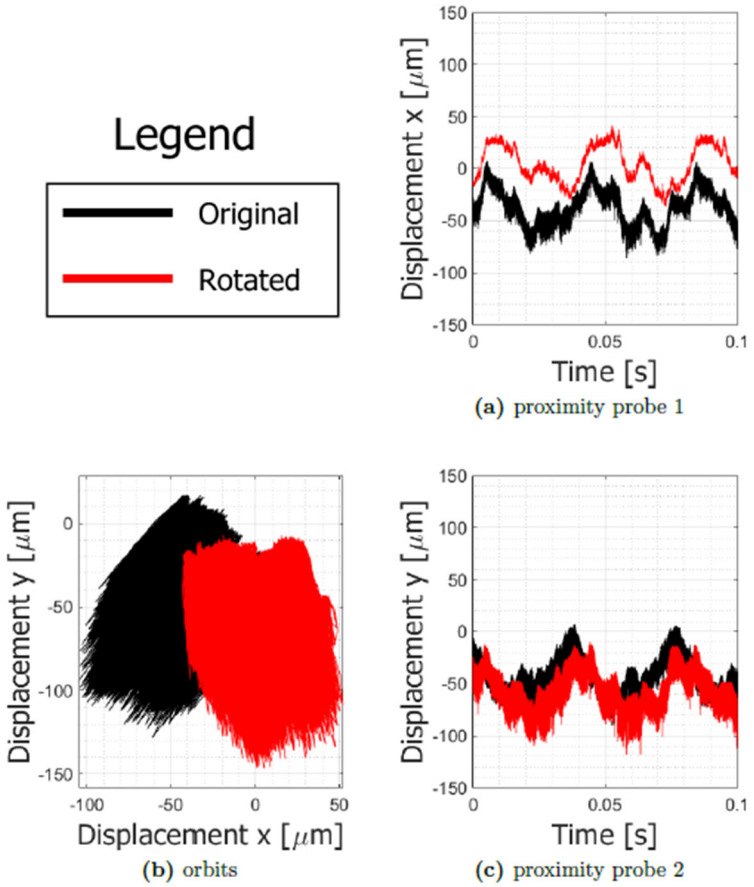

Figure 13. Proximity probe signal rotation example.

As seen for the proximity, acceleration signals also needed to be rotated due to the different reference system. Referring to Figure 12, considering the angle between the reference systems θ equal to 135°, with Equation (2) it was possible to rotate the acceleration time series:

$$\begin{cases} a_x = -a_1 \sin\theta_2 + a_2 \, cos \, \theta_2 \\ a_y = -a_1 \ cos \, \theta_2 - a_2 \, sin \, \theta_2 \end{cases} \quad (2)$$

2.6.2. Steady-State Signal Ranging

This type of post process was applied to all accelerometer signals because the acceleration values developed on the stator axis exceeded those that had been predicted. Consequently, the accelerometers often went into saturation, with a behavior similar to that reported in Figure 14, highlighted with red ellipses.

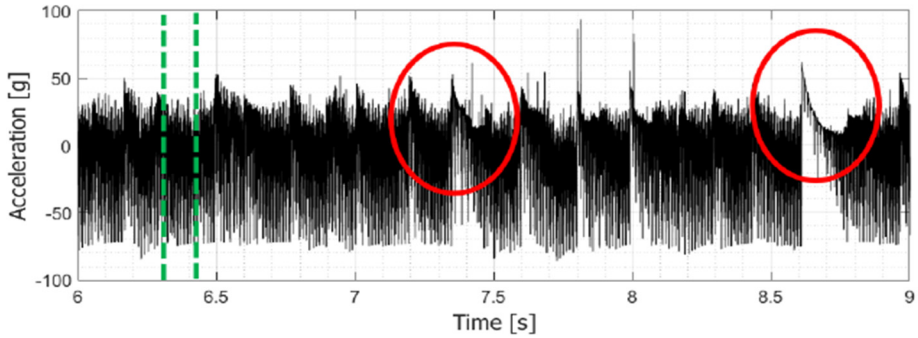

Figure 14. Accelerometer signal saturated time.

For this reason, signal ranging was applied to obtain a steady-state signal. In the example, zooming in on the range defined by dashed green lines, the time series shown in Figure 15 was obtained, useful for frequency-domain consideration.

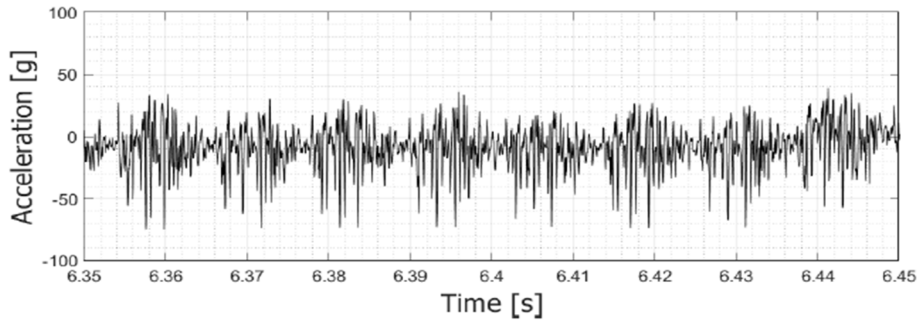

Figure 15. Accelerometer steady-state signal.

2.6.3. Filtering

A filter operation was necessary due to the electrical noise in the signals. During the monitoring of a proximity probe and an accelerometer, both at 0 rpm of the rotor, two high peaks were appreciable, denoting that electrical noise affected the signals at 4000 and 8000 Hz. For this reason, the use of a lowpass filter was a good strategy to remove the noise. A problem arose when supersynchronous frequency components exceeding 4000 Hz were present in the signals (especially in the accelerometers). In these cases, by applying a simple lowpass filter, important parts of the signal were lost. The solution was to apply a multipass filter, trying to remove only the frequencies that represented the noise. The torquemeter was not affected by electrical noise, so no filter was applied. For the displacement signals, the cut frequency for the lowpass filter was between 400 Hz and 1700 Hz, depending on the Fast Fourier Transform (FFT) plot for each test run. For acceleration, as exposed previously, a lowpass filter is not always a good choice to elaborate the signals, especially when the rotation rate is such as to generate supersynchronous frequency components over 4000 Hz. However, in this activity, there were no supersynchronous frequency components and a lowpass filter at 4000 Hz was sufficient to clear the signals of noise.

3. Experimental Results and Discussions

The tested configurations of the test rig were Horizontal "Baseline" (HB), Vertical "Baseline" (VB), Vertical "Low Clearance" (VL) and Vertical "High Clearance" (VH). Geometrical and inertial properties of the tested configurations are reported within Table 3 while Figure 16 illustrates the drawings of the radial PCD inner ring for baseline and low/high clearance configurations.

Table 3. Some geometrical and inertial properties for the tested configurations.

Parameter		HB	VB	VL	VH
Rotor Mass	[kg]	55	61	63	63
Rotor Polar Inertia	[kg·m^2]	1.26	1.31	1.34	1.34
Rotor Diametral Inertia	[kg·m^2]	0.66	0.72	0.77	0.77
Radial Clearance	[μm]	50	50	40	200
PCD Statoric Mass	[kg]	0.517	0.517	3.103	3.103
Pad Rows Distance	[m]	0.029	0.029	0.029	0.029
Rotor–Stator Interface Radius	[m]	0.039	0.039	0.052	0.052
Female PCD Ring Pad Number	[−]	22	22	31	31
Male PCD Ring Pad Number	[−]	21	21	30	30

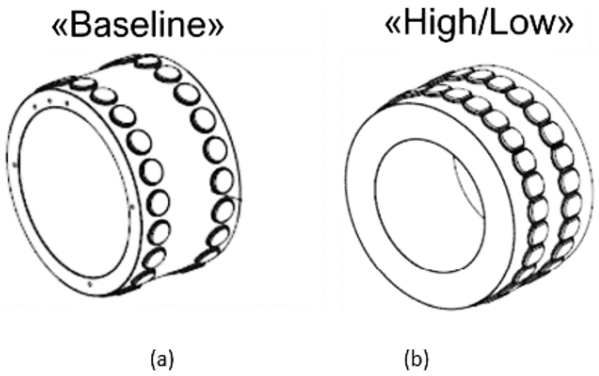

Figure 16. Bearing drawings: (**a**) baseline and (**b**) high/low clearance configurations.

In addition to the masses and inertias of the rotor, among the geometric features of the bearing, it is necessary to highlight the different radial clearances and the different number of pads, which modify accelerometer signals in terms of frequency and amplitude. Firstly, some useful comparisons between configurations are presented in terms of orbits, mean and peak-to-peak values and frequency spectrum, in the function of rotational speed.

3.1. Comparison of Horizontal "Baseline" vs. Vertical "Baseline"

These two configurations were different just for the effect of gravity acceleration and the rotor mass and inertia. The PCD bearing mounted was the same, with the same geometrical characteristics. Time and frequency domains are discussed in detail in the following paragraphs. The same approach is adopted for both configurations analyzed.

3.1.1. Time-Domain Analysis

A comparison between the orbits for the tested configuration is reported in Figure 17. The dashed blue line, representing the clearance circle, is centered in the nominal axis of the stator. This circle is just a representation; the real center depends on the stator deformation. In black are shown the results for the Horizontal "Baseline" case, while in red are those for the Vertical "Baseline". The effect of gravity is evident at all revolution speeds. Furthermore, the shape of the orbits is different; in particular, the horizontal configuration has a preferential area of rubbing due to gravity which, at lower rotation speeds, pulls the rotor downwards. Beyond a certain speed, the orbit has a shape very similar to that of the vertical configuration, always maintaining a downward translation.

Considering now the torque absorption, for which the mean values versus rotational speed for both the configurations are reported in Figure 18, it can be noted that up to 1000 rpm the vertical configuration has the lower absorption. In the range from 1500 to 3500 rpm, the average value is about the same, followed by a marked increase over 4000 rpm, in which the vertical configuration comes to absorb an additional 25% in respect to the horizontal one. This increase is mainly justified by the fact that the vertical configuration requires a thrust PCD bearing, which also absorbs a fair amount of torque. The

higher values of the horizontal configuration at low speeds depend probably on the type of contact: at this speed there are many impulses were generated by high frictional forces.

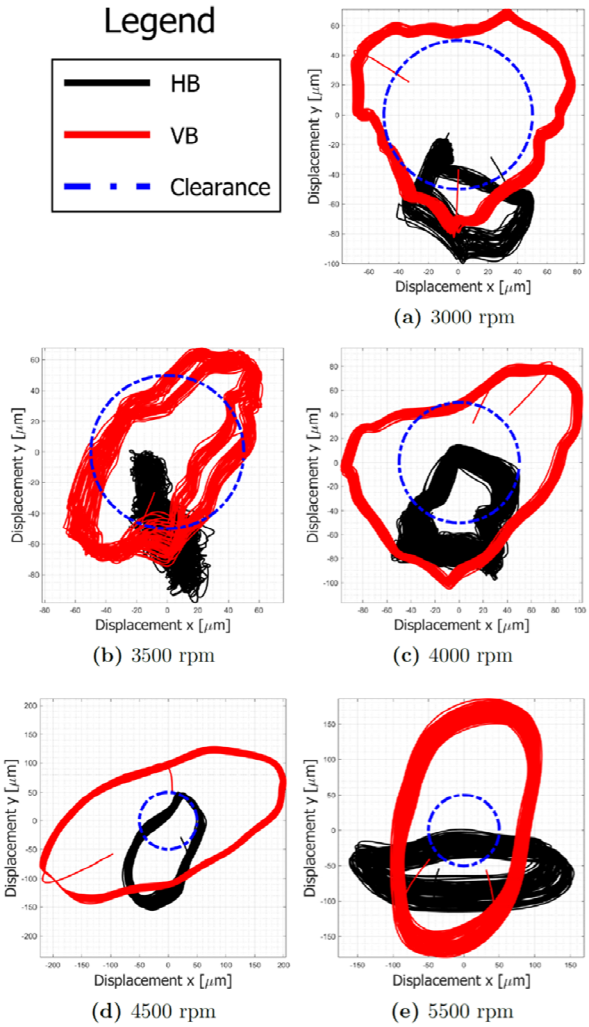

Figure 17. Orbit comparison between Horizontal "Baseline" and Vertical "Baseline".

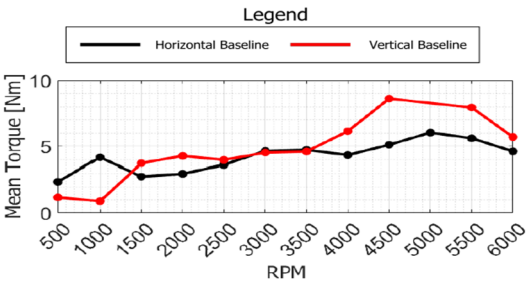

Figure 18. Torque mean value comparison between Horizontal "Baseline" and Vertical "Baseline".

3.1.2. Frequency-Domain Analysis

Now the signals from the proximitor, accelerometer and torquemeter will be analyzed using a frequency spectrum cascade. Considering the proximitor signals, reported in Figure 19a and Figure 19b for the Horizontal "Baseline" and Vertical "Baseline", respectively, it can be observed that the main frequency of the components is represented by the synchronous frequency, for both configurations. In some speed runs, the rise in the x2 component is visible, but always lower than x1.

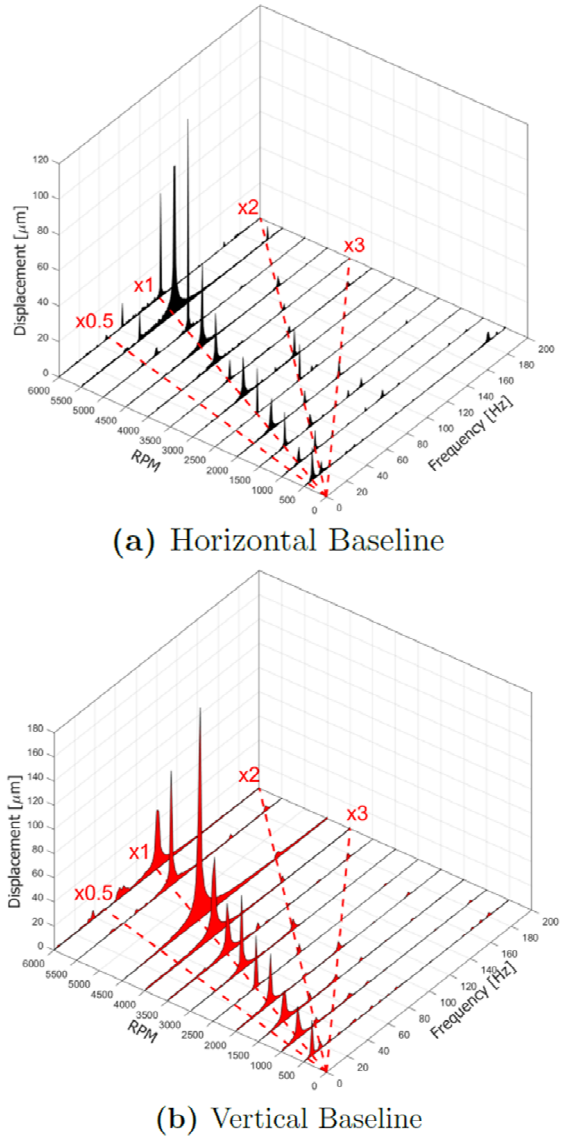

(a) Horizontal Baseline

(b) Vertical Baseline

Figure 19. Frequency spectrum cascade comparison for proximitor.

Turning to accelerations and remembering that the number of pads for the PCD bearing is 21 for the male and 22 for the female ring, we can easily see how the main frequency components are multiples of the number of pads. Waterfall diagrams are visible in Figure 20a and Figure 20b for the Horizontal "Baseline" and Vertical "Baseline", respectively. Lower synchronous components (such as x1, x2 etc.) are not evident at speeds lower than 3000 rpm. Some of them appear from 3500 rpm, but always with an amplitude lower than the pad multiple.

To compare the configurations at different revolution speeds, FFT areas are plotted in Figure 21. Assuming that the acceleration is a measure of the force exchanged during the contact of the PCD bearing, and therefore a measure of the dynamic stress induced by the rotor, it can be observed that the accelerations are lower for the Vertical "Baseline" configuration up to 3500 rpm, where they go over those of the horizontal configuration. Subsequently, immediately after 5000 rpm, the vertical configuration shows a better behavior.

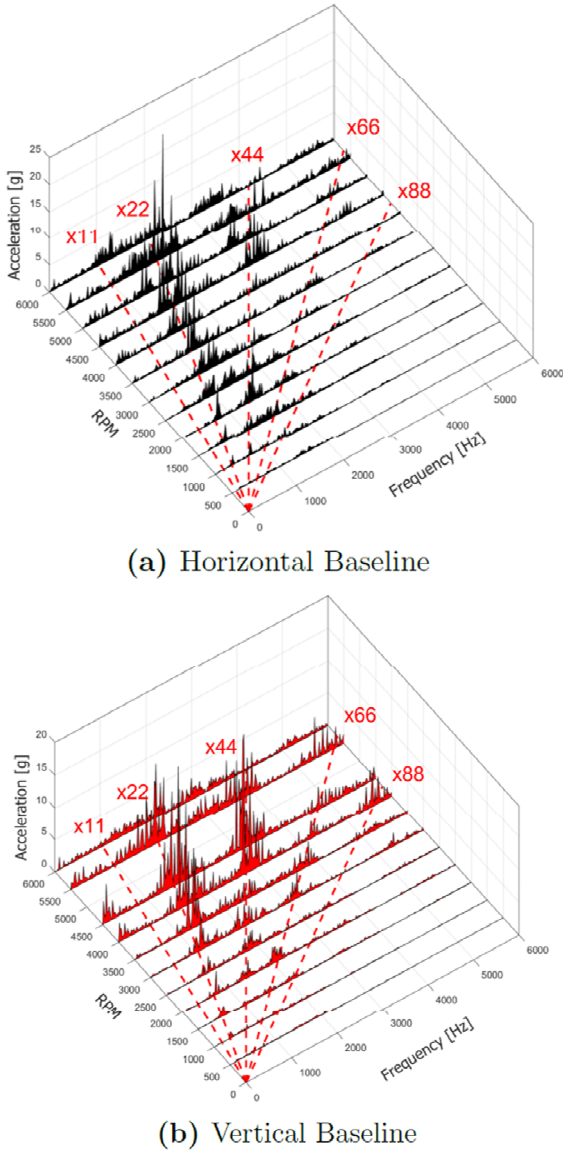

(a) Horizontal Baseline

(b) Vertical Baseline

Figure 20. Frequency spectrum cascade comparison for accelerometer.

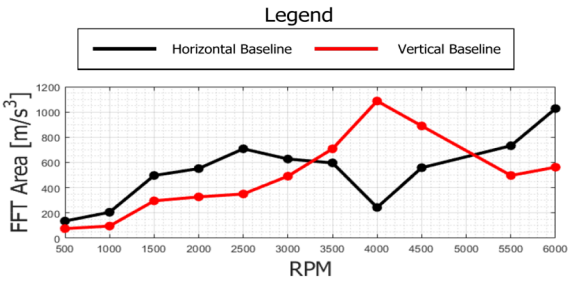

Figure 21. Acceleration FFT area comparison.

Focusing on some working speeds, frequency spectra comparison is shown in Figure 22. Conforming to the trend described in Figure 21, at 3500 and 4500 rpm vertical peaks are somewhat higher than the horizontal ones. Instead, at 5500 rpm the accelerometer in the x direction for the horizontal configuration shows a pad synchronous peak higher than that of the vertical configuration. Looking at the torque absorption in Figure 23a,b for the Horizontal "Baseline" and Vertical "Baseline", respectively, the behavior is a little bit different for each configuration. In particular, for the HB, the main frequency component is

the synchronous one but from 3500 rpm x2 arise until they become higher than x1. In one case, at 4000 rpm, the x3 component is higher than x1 and x2. Finally, at 3000 rpm, x4 is higher than x1. Instead, for VB, x1 increases linearly with the revolution speed except for 6000 rpm. x2 is almost always present, and higher than x1 just from 3000 to 4000 rpm. x3 is present and the highest at 2500 rpm.

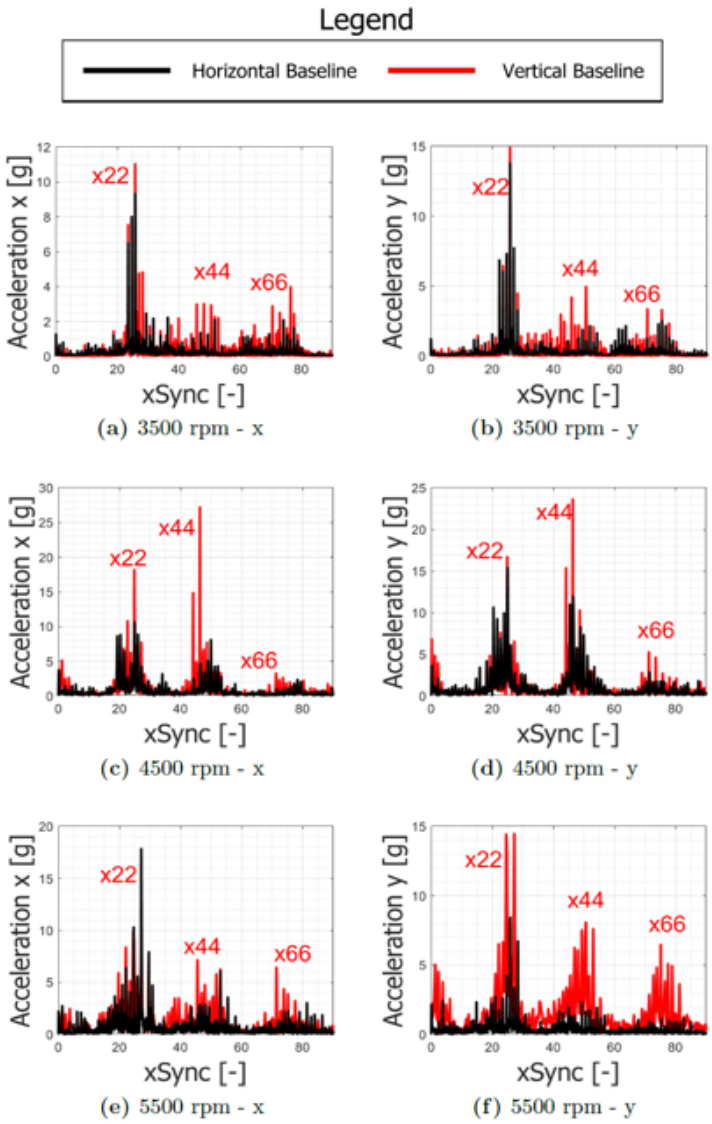

Figure 22. Frequency spectrum comparison for Horizontal and Vertical Baseline.

3.2. Comparison of Vertical "Baseline", "Low" and "High"

These three configurations were different just for the radial clearance, which was equal to 50 µm for the Vertical "Baseline", 40 µm for the Vertical "Low" and 200 µm for the Vertical "High".

3.2.1. Time-Domain Analysis

A comparison between the orbits normalized with respect to the radial clearance for the three tested configurations is visible in Figure 24. The "Baseline", "Low" and "High" clearance vertical configurations, respectively, are represented in the solid red, blue and green lines. The black dashed circle line represents the normalized clearance circle. For VB, a preferential direction of stretching for the orbit is quite clear, while the VL and VH orbits are much more circular. From 3000 rpm, the VH orbit is quite chaotic in comparison to the

other two, but always circular-shaped. In Figure 25 are shown the mean torque absorptions for the three configurations. All of them have the same axial PCD bearing, so it is possible to perform a direct comparison. All of the mean values get higher the higher the revolution speed. A geometrical parameter that affects this measure is the rotor–stator interface radius; look at Table 3. For the lower value of the interface radius (39 mm), VB has generally the lower mean torque absorption. The other two configurations have the same interface radius (52 mm); for 500 and 1000 rpm, the lower value for VH can be justified because the stiffness of the metal bellows draws the rotor to the center, avoiding contact. For higher revolution speeds, the mean torque is almost the same for both the VL and VH configurations.

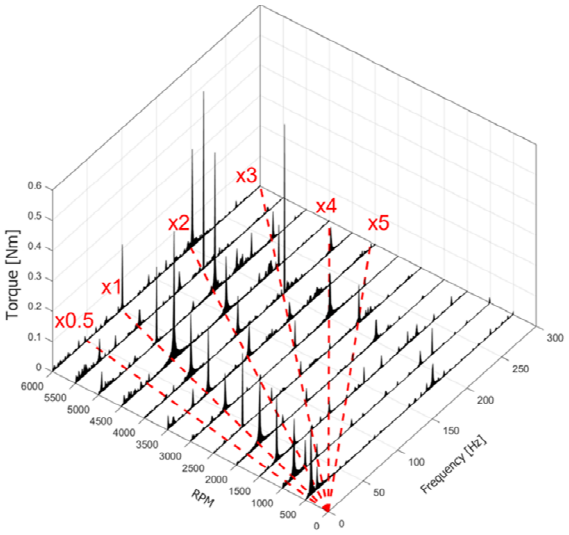

(a) Horizontal Baseline

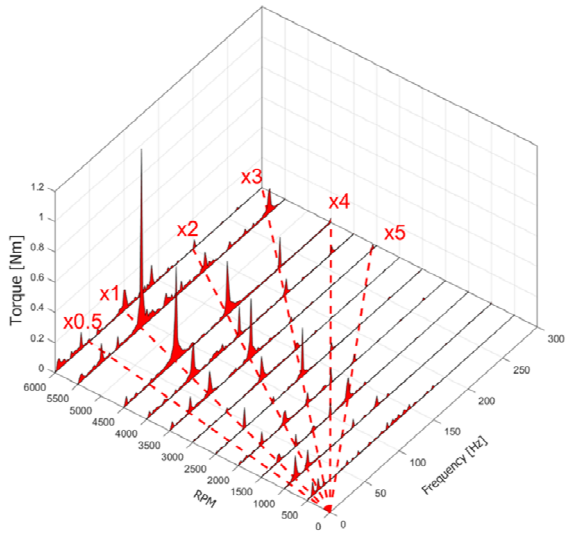

(b) Vertical Baseline

Figure 23. Frequency spectrum cascade comparison for torquemeter.

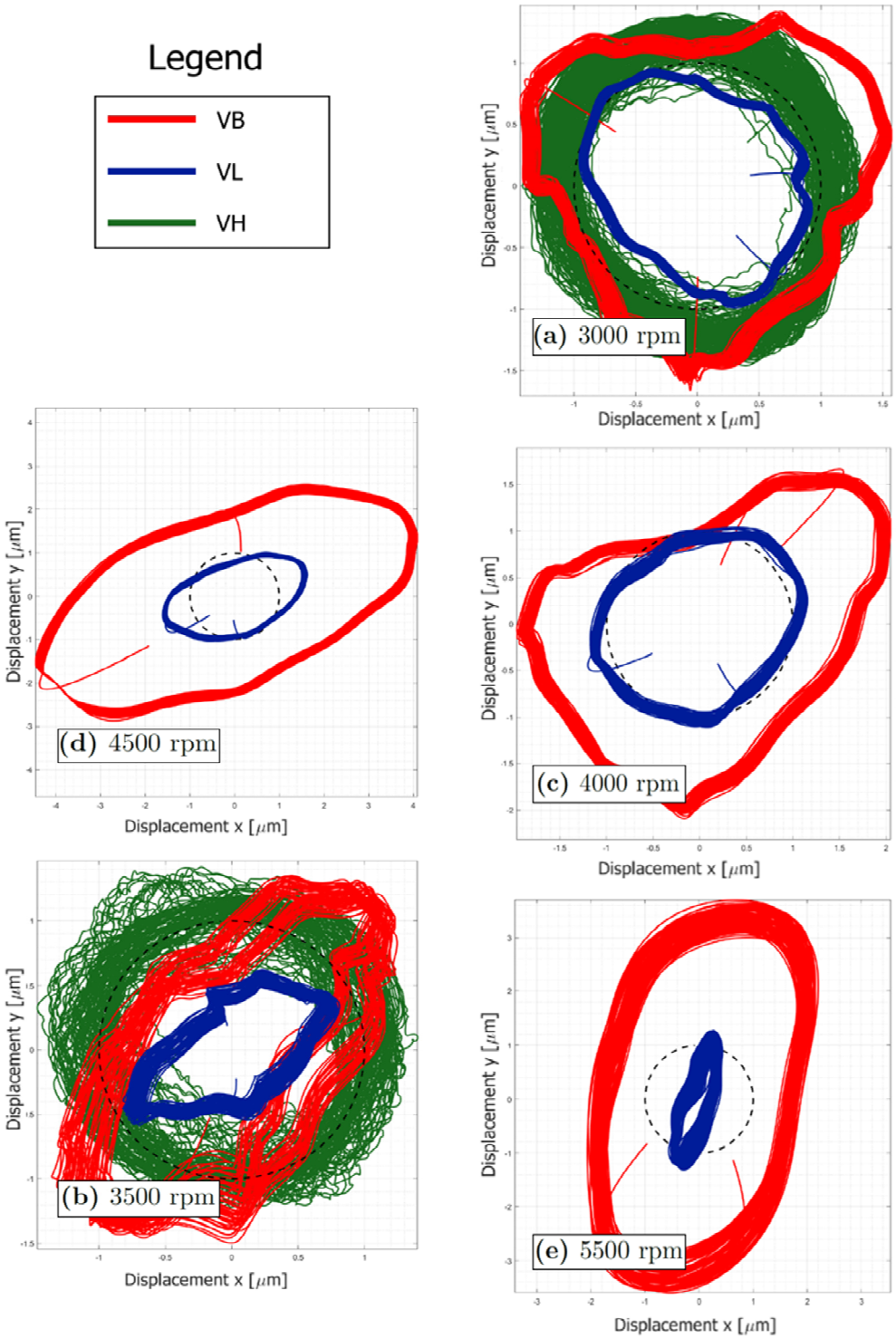

Figure 24. Orbit comparison between Vertical "Baseline", "Low" and "High" clearance.

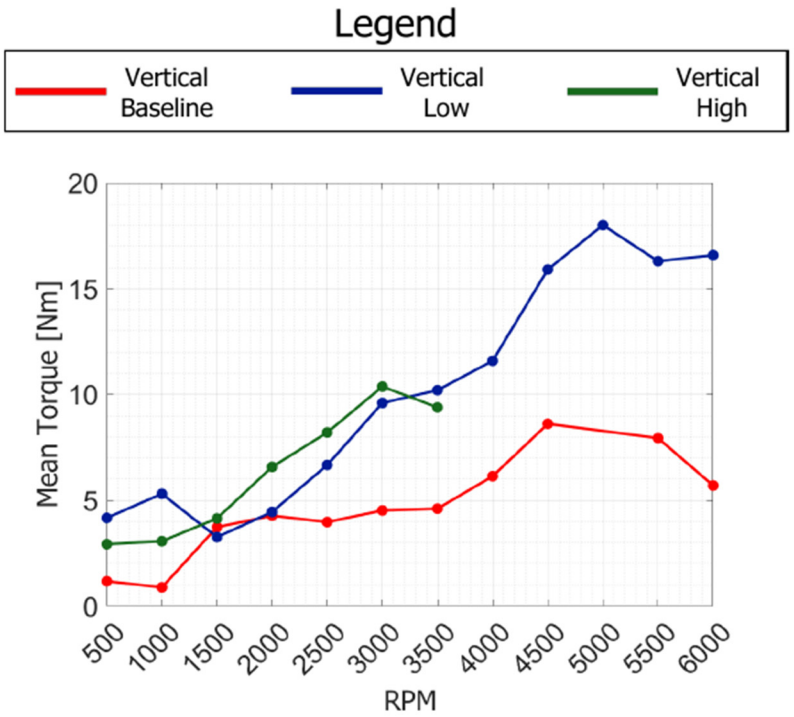

Figure 25. Torque mean value comparison between Vertical "Baseline", "Low" and "High" clearance.

3.2.2. Frequency-Domain Analysis

Now the signals from the proximitor, accelerometer and torquemeter will be analyzed using the frequency spectrum cascade. Considering the proximitor signals, reported in Figure 26 for all vertical configurations, it is possible to see that the main frequency component is represented by the synchronous peak. The High clearance configuration does not experience any supersynchronous frequency components, while, at a higher speed, the spectrum suggests an extreme shock and chaotic motion. For the "baseline" and "low" configurations, in some speed runs it a rise in the x2 component can be observed, always lower than that of x1. Concerning the accelerations, in Figure 27 the comparison between the FFT area is shown, in order to evaluate which configuration is the most critical considering the stator dynamic load. At the lower speeds (500 and 1000 rpm) the "high" clearance configuration is near zero in acceleration. When impact occurs, from 1500 to 2500 rpm, "high" overcomes "low" clearance. Over 3000 rpm, "high" clearance is the highest in terms of acceleration's FFT area. It is evident that clearance really affects the stator–rotor force interaction.

In Figure 28 are shown the waterfall diagrams for the three configurations. It is theoretically plausible that the supersynchronous components derive from the pad number. Remembering Table 3 and looking at the pad number, the Vertical "Baseline" configuration experiences x22, in strong accordance with this theory. On the other hand, the "low" and "high" configurations, despite a number of pads of 25 for the male ring and 26 for the female ring, experience multiple x30, x60 and x90. Frequency spectra comparison for the three configurations at the main running speeds (3000, 3500, 4000, 4500, 5500 and 6000 rpm) are shown in Figure 29. Interestingly, the VB configuration experiences the highest accelerations up to 6000 rpm, where there is a drastic reduction in peaks. The VH configuration has the lowest peaks. This is probably due to the increased clearance that permits the metal bellows to slow down the rotor before impact.

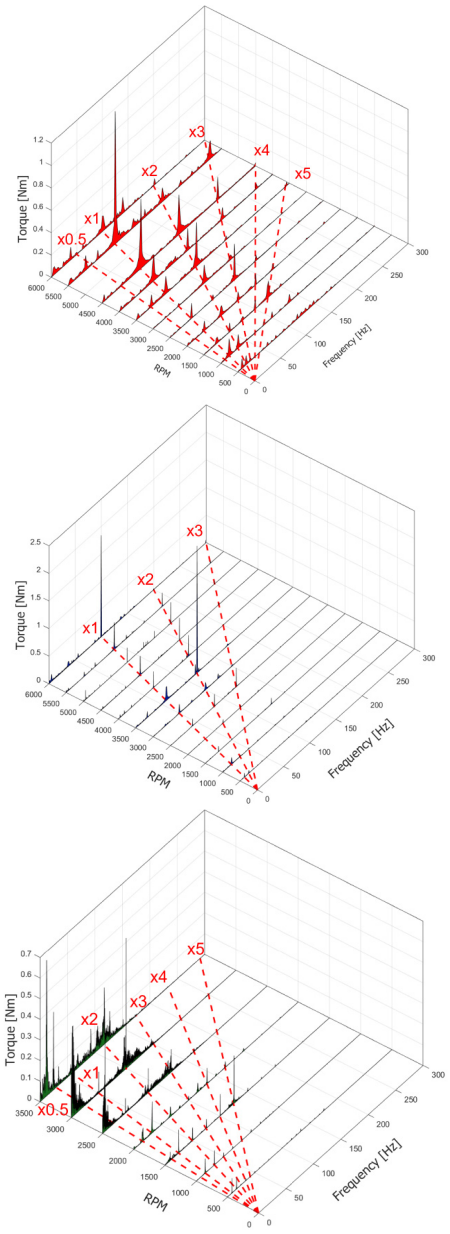

Figure 26. Frequency spectrum cascade comparison for proximity probe (Vertical Baseline, Vertical Low and Vertical High).

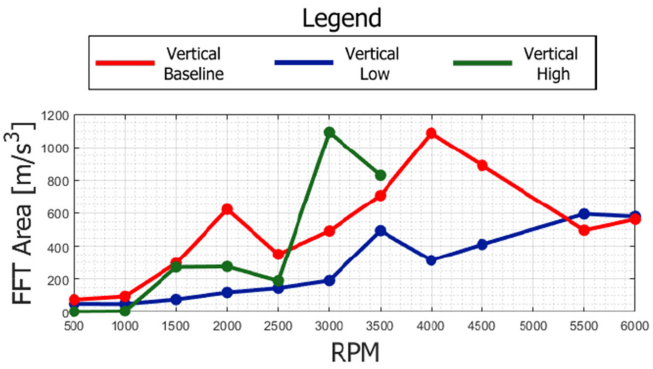

Figure 27. Acceleration FFT area comparison between Vertical "Baseline", "Low" and "High" clearance.

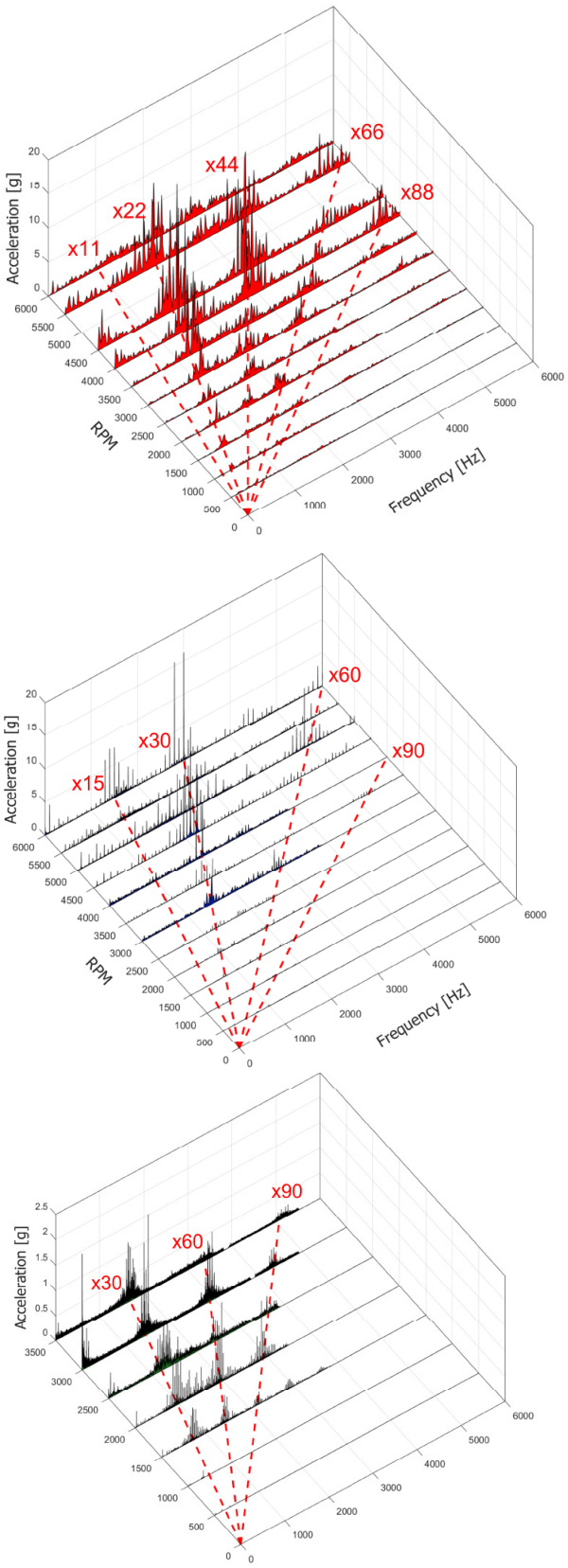

Figure 28. Frequency spectrum cascade comparison for accelerometer (Vertical Baseline, Vertical Low and Vertical High).

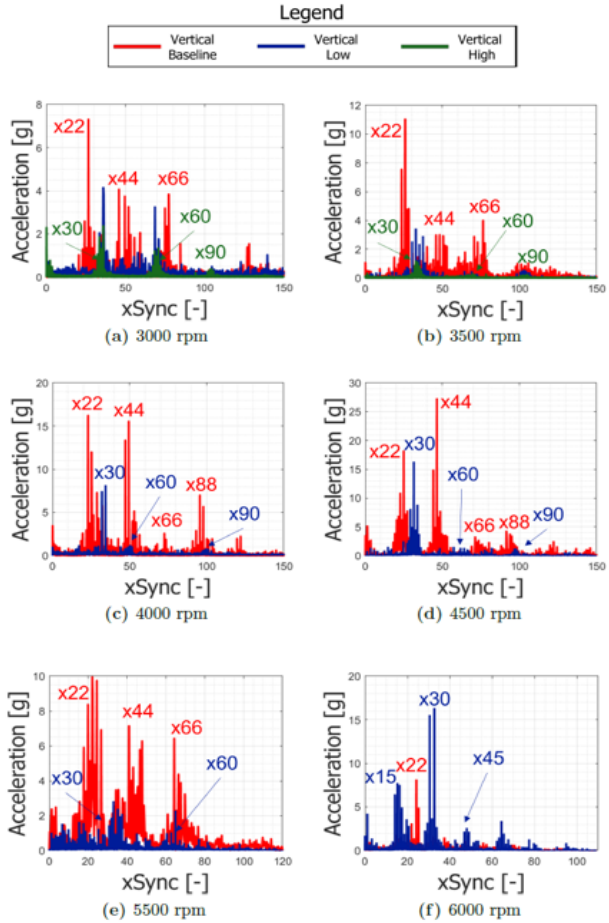

Figure 29. Frequency spectrum cascade comparison for "Vertical Baseline", "Vertical Low" and "Vertical High".

At 3000 rpm, this trend reverses and VL has peaks greater than VH. At the overspeed of 6000 rpm, the "low" clearance configuration has the highest acceleration peak at x30, and x15 and x45. Passing now to the torque absorption, depicted in Figure 30, VH has a more chaotic frequency spectrum, probably caused by the high-impact frequency. At 1500 rpm, it is possible to see the higher peak at the x5 supersynchronous component. VL has a cleaner behavior. The synchronous component is always similar to x2 except for 6000 rpm where it is higher. At 3500 rpm, the highest peak appears at the x3 supersynchronous component.

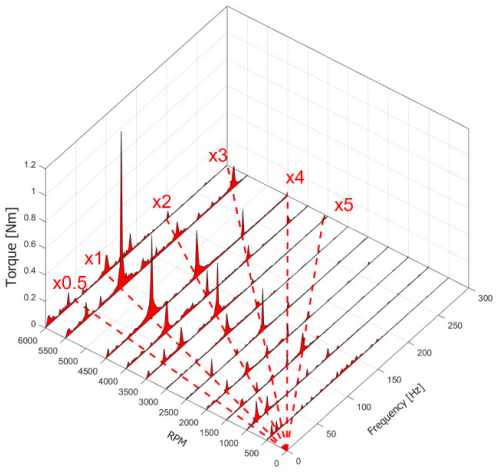

Figure 30. *Cont.*

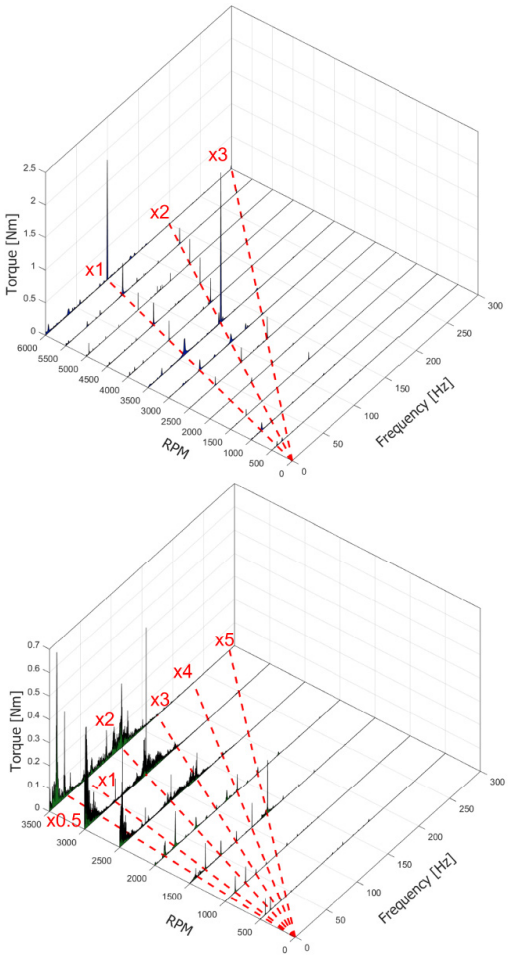

Figure 30. Frequency spectrum cascade comparison for torquemeter (Vertical Baseline, Vertical Low and Vertical High).

4. Conclusions and Future Developments

In the present activity, a rotor dynamics test bench was designed and instrumented to study the behavior of a turbomachinery rotor resting on innovative polycrystalline diamond (PCD) plain bearings. The aim of the work was to acquire the orbits, stator accelerations and absorbed torque for various types of bearings ("Baseline", "Low" and "High") in various configurations ("Horizontal" and "Vertical") and consequently carry out comparisons between them. Much experimental data was acquired. As for the experimental results, within this paragraph the comparisons between the reference configurations are discussed.

4.1. Horizontal Baseline vs. Vertical Baseline

The behavior of the vertical configuration is certainly more stable due to the nature of the continuous contact present between the rotor and stator, which generates more "common" orbits in rotor dynamics. On the other hand, the horizontal configuration presents an intermittent contact at lower speeds and consequently the generated acceleration results were higher. However, it is extremely important to take into account the dynamic behavior of the stator, as any unexpected resonances could increase the order of magnitude of the accelerations and consequently compromise the operation of the machine, even if apparently the behavior could be quieter. From a frequency-domain point of view, the presence of a supersynchronous multiple of the number of pads was immediately noticed. These peaks very often turned out to be higher than the synchronous ones, and therefore must necessarily be taken into consideration in the design phase. As far as the absorbed torque is concerned, the configurations are essentially the same. Considering that in the Vertical Baseline configuration there is an additional PCD thrust bearing, below 3500 rpm

the torque of the Vertical Baseline is lower than that of the Horizontal Baseline. This can be explained by the nature of continuous contact which reduces the frictional force compared to intermittent contact. At high speeds, when the nature of the contact is the same (and therefore the orbits are almost elliptical), the Vertical Baseline absorbs more power due to the axial PCD.

4.2. Vertical Baseline vs Vertical Low vs. Vertical High

With the same orientation, the main difference between these configurations consists in the interface radius between the rotor and stator and the radial clearance present in the PCD bearings; the latter is the parameter that, in this case, distinguishes the type of contact (with the same unbalance and rotation speed). From the orbits, it can be deduced that for the Vertical Low and Vertical Baseline configurations, the behavior is stable with continuous contact, at least at industrially useful speeds. In the Vertical High configuration, on the other hand, since there is a lot of radial gap available, the rotor comes into contact only from 1000 rpm upwards. Consequently, its behavior is very unstable and with intermittent contact. As for the accelerations, we have seen how the Vertical Baseline presents higher accelerations, especially from 3000 rpm onwards. In the frequency domain, the presence of a supersynchronous multiple of the number of pads is still evident. Finally, with regard to the absorbed torque, it was immediately clear that the fundamental difference is caused by the interface radius between the rotor and stator.

As an extension to the present study, the definition of an effective numerical model for the prediction of the test rig performance will represent the most important development. This will be essential to make the global method more effective and faster. In addition, the high modularity of the system could allow the testing of several and different working conditions, with the objective to extend the adoption of the PCD bearing to other turbomachinery applications.

Author Contributions: Conceptualization, A.C. and A.A.; Methodology, A.C., A.A. and E.M.; Software, A.C. and A.A.; Validation, A.C.; Resources, E.M. and A.R.; Data curation, A.A.; Writing—original draft, A.C.; Writing—review & editing, E.M.; Supervision, E.M. and A.R.; Project administration, A.R. All authors have read and agreed to the published version of the manuscript.

Funding: This research received no external funding.

Institutional Review Board Statement: Not applicable.

Informed Consent Statement: Not applicable.

Data Availability Statement: The original contributions presented in the study are included in the article, further inquiries can be directed to the corresponding author.

Acknowledgments: This study was supported by the MOST Sustainable Mobility National Research Center and received funding from the European Union Next Generation EU (PIANO NAZIONALE DI RIPRESA E RESILIENZA (PNRR) MISSIONE 4 COMPONENTE 2, INVESTIMENTO 1.4 D.D. 1033 17/06/2022, CN00000023).

Conflicts of Interest: The authors declare no conflicts of interest.

References

1. Barnard, A.S. *The Diamond Formula: Diamond Synthesis: A Gemmological Perspective*; Butter-worth-Heinemann: Oxford, MA, USA, 2000.
2. Donoghue, M. *Gems: Their Sources, Descriptions and Identification*; Butterworth-Heinemann: Oxford, MA, USA, 2006.
3. Spear, K. *Synthetic Diamond: Emerging CVD Science and Technology*; Wiley: New York, NY, USA, 1994.
4. US Synthetic (CHAMPION X), PCD Drilling Tools. Available online: https://www.championx.com/products-and-solutions/drilling-technologies/diamond-bearings (accessed on 5 June 2024).
5. Lingwall, B.; Sexton, T.; Cooley, C. Polycrystalline diamond bearing testing for marine hydrokinetic application. *Wear* **2013**, *302*, 1514–1519. [CrossRef]
6. Knuteson, C.; Sexton, T.; Cooley, C. Wear-in behavior of polycrystalline diamond thrust bearings. *Wear* **2011**, *271*, 2106–2110. [CrossRef]

7. Sexton, T.; Cooley, C. Polycrystalline diamond thrust bearings for down-hole oil and gas drilling tools. *Wear* **2009**, *267*, 1041–1045. [CrossRef]
8. Bromaghin, A.; Ali, M.; Ravens, T.; Petersen, T.; Hoffman, J. Experimental study of abrasion characteristics for critical sliding components for use in hydrokinetic devices. *Renew. Energy* **2014**, *66*, 205–214. [CrossRef]
9. Cooley, C.; Khonsari, M.; Lingwall, B. *The Development of Open Water-Lubricated Polycrystalline Diamond (PCD) Thrust Bearings for Use in Marine Hydrokinetic (MHK) Energy Machines*; Technical Report; US Synthetic Bearings: The Woodlands, TX, USA, 2012.
10. Dykas, B.; Bruckner, R.; DellaCorte, C.; Edmonds, B.; Prahl, J. Design, Fabrication, and Performance of Foil Gas Thrust Bearings for Microturbomachinery Applications. *J. Eng. Gas Turbines Power* **2008**, *131*, 012301. [CrossRef]
11. Andrés, L.S.; Phillips, S.; Childs, D. A Water-Lubricated Hybrid Thrust Bearing: Measurements and Predictions of Static Load Performance. *J. Eng. Gas Turbines Power* **2016**, *139*, 022506. [CrossRef]
12. Norrbin, C.S.; Childs, D.W. Lateral Equilibrium Position Analysis Program with Applications to Electric Submersible Pumps. *J. Eng. Gas Turbines Power* **2018**, *140*, 38482. [CrossRef]
13. Norrbin, C.S.; Childs, D.W.; Phillips, S. Including Housing–Casing Fluid in a Lateral Rotordynamics Analysis on Electric Submersible Pumps. *J. Eng. Gas Turbines Power* **2017**, *139*, 062505. [CrossRef]
14. Gilardi, G.; Sharf, I. Literature survey of contact dynamics modelling. *Mech. Mach. Theory* **2002**, *37*, 1213–1239. [CrossRef]
15. Machado, M.; Moreira, P.; Flores, P.; Lankarani, H.M. Compliant contact force models in multibody dynamics: Evolution of the Hertz contact theory. *Mech. Mach. Theory* **2012**, *53*, 99–121. [CrossRef]
16. Skrinjar, L.; Slavič, J.; Boltežar, M. A review of continuous contact-force models in multibody dynamics. *Int. J. Mech. Sci.* **2018**, *145*, 171–187. [CrossRef]